Reproducing ~~springtime~~ Arctic springtime tropospheric ozone and mercury depletion events in an outdoor mesocosm sea-ice facility

Zhiyuan Gao[1], Nicolas-Xavier Geilfus[1], Alfonso Saiz-Lopez[2], and Feiyue Wang[1]

[1]Centre for Earth Observation Science, and Department of Environment and Geography, University of Manitoba, Winnipeg, MB R3T 2N2, Canada
[2]Department of Atmospheric Chemistry and Climate, Institute of Physical Chemistry Rocasolano, CSIC, 28006 Madrid, Spain

Correspondence: Feiyue Wang (feiyue.wang@umanitoba.ca)

Abstract. The episodic build-up of gas-phase reactive bromine species over sea ice and snowpack in the springtime Arctic plays an important role in ~~the~~ boundary layer processes, causing annual concurrent depletion of ozone and gaseous elemental mercury (GEM) during polar sunrise. Extensive studies have shown that these phenomena, known as bromine explosion events (BEEs), ozone depletion events (ODEs) and mercury depletion events (MDEs), respectively, are all triggered by gas-phase reactive bromine species that are photochemically activated from bromide via multi-phase reactions under freezing air temperatures. However, major knowledge gaps exist in both fundamental cryo-photochemical processes causing these events and meteorological conditions that may affect their timing and magnitude. Here, we report an outdoor mesocosm ~~scale~~ study in which we successfully reproduced ODEs and MDEs at the Sea-ice Environmental Research Facility (SERF) in Winnipeg, Canada. By monitoring ozone and GEM concentrations inside large, acrylic tubes over bromide-enriched artificial seawater during ~~entire~~ sea ice freeze-and-melt cycles, we observed mid-day photochemical ozone and GEM loss in winter in the in-tube boundary layer air immediately above the sea ice surface in a pattern that is characteristic of BEE-induced ODEs and MDEs in the Arctic. The importance of UV radiation and the presence of a condensed phase (experimental sea ice or snow) in causing such reactions ~~surface ozone loss~~ was demonstrated by comparing ozone and GEM concentrations between the UV-transmitting and UV-blocking acrylic tubes under different air temperatures. The ability of reproducing BEE-induced ~~ODEs~~ photochemical phenomena in ~~at~~ a mesocosm ~~scale~~ in a non-polar region provides a new approach to systematically studying the cryo-photochemical processes and meteorological conditions ~~processes~~ leading to BEEs, ODEs, and MDEs in the Arctic, their role in biogeochemical cycles across the ocean-sea ice-atmosphere interface~~s~~, and their sensitivities to climate change.

1 Introduction

Every year during springtime in the Arctic, a series of episodic photochemical events is ~~are~~ observed concurrently in the boundary layer air, including bromine explosion events (BEEs), ozone depletion events (ODEs), and mercury depletion events (MDEs) (Barrie et al., 1988; Barrie and Platt, 1997; Bottenheim et al., 1986; Oltmans et al., 1989; Oltmans and Komhyr, 1986;

Platt and Hausmann, 1994; Schroeder et al., 1998; Steffen et al., 2005). Subsequent studies have shown that these events are triggered by the rapid cycling of photolytically activated halogen species (especially bromine species such as Br, BrO, HOBr), giving rise to BEEs) over sea ice or snowpack surface, which rapidly react with ozone and gaseous elemental mercury (GEM) in the boundary layer air, resulting in ODEs and MDEs (Abbatt et al., 2012; Bognar et al., 2020; Pratt et al., 2013; Saiz-Lopez and von Glasow, 2012; Simpson et al., 2007b; Wang et al., 2019). These annually recurring photochemical processes greatly change the oxidative conditions of the Arctic marine boundary layer during springtime, affecting biogeochemical cycles of many inorganic and organic chemicals across the ocean-sea ice-atmosphere interfaces in the Arctic (Wang et al., 2017).
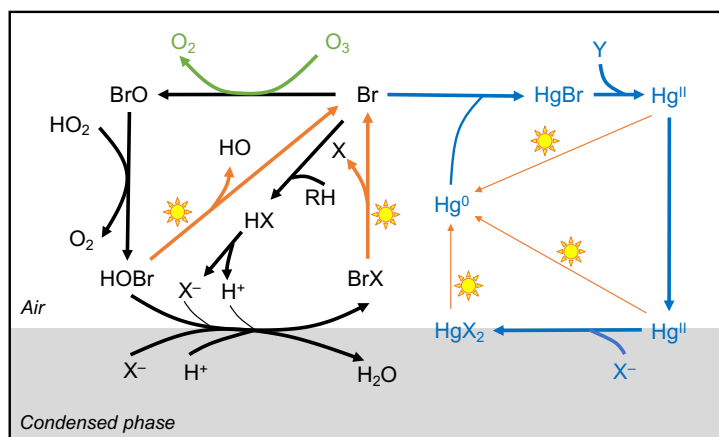
Figure 1. General reaction schemes involved in bromine explosion events, ozone depletion events and mercury depletion events in the Arctic during polar sunrise. The photochemical activation of~~:~~ gas-phase reactive bromine species (Br and BrO) produced from multi-phase reactions on the surface of the condensed phase ~~will~~ causes the depletion of ozone and gaseous elemental mercury in the boundary layer air (based on Abbatt et al., 2012; Khiri et al., 2020; Saiz-Lopez and von Glasow, 2012; Simpson et al., 2007b, 2015; Wang et al., 2017; Wang and Pratt, 2017).

While there is a general consensus on the reaction schemes involved in BEEs, ODEs and MDEs (Fig. 1), major uncertainties exist with respect to the fundamental cryo-photochemical processes causing these events and meteorological conditions that may affect their timing and magnitude. ~~For instance, the initiation step is thought to be a multi-phase (mp) oxidation of halide by HOBr presumably on the surface of a saline condensed phase (Abbatt et al., 2012; Simpson et al., 2007, 2015):~~

It has been generally assumed that the cycling of reactive bromine species is sustained by HOBr and BrONO$_2$ via multi-phase reactions on the surface of a condensed phase during polar sunrise (Abbatt et al., 2012; Simpson et al., 2007b, 2015; Wang and Pratt, 2017). ~~X⁻ + HOBr + H⁺ mp→ H₂O + BrX   (R1)~~

~~where X = Br or Cl.~~ Yet the role of HOBr and the nature of the condensed phase remain~~s~~ not well characterized. Some studies have suggested a potential link between bromine activation and the extent of first-year and multi-year sea ice (Bognar et al., 2020; Simpson et al., 2007a), whereas field observations and laboratory studies show that s~~S~~aline snowpack~~, first-year and multi-year sea ice, frost flowers~~ and sea salt aerosols are ~~have all been proposed to~~ more likely to provide such a condensed phase for the reactions (Huff and Abbatt, 2002~~Bognar et al., 2020~~; Pratt et al., 2013; ~~Simpson et al., 2007, 2015;~~ Wang et al., 2019; Wren et al., 2013; Xu et al., 2016). The cycling of bromine species ~~However, as Reaction (R1)~~ is favoured under acidic conditions (Halfacre et al., 2019; Pratt et al., 2013), and~~,~~ the surfaces of sea ice and frost flowers, which are highly alkaline (Hare et al., 2013), are unlikely to be effective in ~~initiating~~ sustaining the reactions. Bromine activation also requires solar radiation, especially in the UV region, and is affected by air temperatures, as BEEs, ODEs and MDEs are only observed during polar sunrise and diminished when the air temperature rises to above 0 °C (Bognar et al., 2020; Burd et al., 2017; Steffen et al., 2005). Atmospheric and sea-state conditions, such as air mass origin, sea ice and boundary layer dynamics, and blowing snow events, may also affect the timing and magnitude of BEEs, ODEs and MDEs (Bognar et al., 2020; Moore et al., 2014; Thomas et al., 2011; Zhao et al., 2016).

So far most of the studies on BEEs, ODEs and MDEs are based on field observations, which reflect integrated complex processes occurring in nature, but the lack of controllability makes it difficult to address some of the aforementioned knowledge gaps on the fundamental cryo-photochemical processes. The logistics of field campaigns also pose restrictions on the chemical species that can be measured and the nature and dynamics of the sea ice environment that can be studied. To help elucidate fundamental processes, laboratory studies have been conducted to study the halogen release mechanism~~s~~ from frozen

70 saline solutions (Abbatt et al., 2010; Huff and Abbatt, 2002; Sjostedt and Abbatt, 2008). Such frozen saline solutions may chemically resemble Arctic sea ice or snow substrates, but the laboratory-based studies cannot reproduce the natural growth of sea ice, nor the atmospheric and sea-state conditions. In this study, we present a mesocosm ~~scale~~ experiment to investigate the occurrence and magnitude of BEE-induced ODEs and MDEs. The experiment covered several freeze-and-melt cycles of experimental sea ice and open water periods. The temporal changes in ~~surface~~ ozone and GEM concentrations were~~was~~

75 monitored in the boundary layer air mass inside acrylic tubes. Simultaneous p~~P~~hotochemical depletions of ~~surface~~ ozone ~~loss~~ and GEM under freezing air temperatures were observed in agreement with the characteristics of BEE-induced ~~ODEs~~photochemical phenomena. We show that the experimental design provides a new mesocosm platform to study ~~mesocosm-scale~~ BEEs, ODEs and MDEs, which will help elucidating fundamental processes behind their occurrence in the Arctic and their sensitivity to climate change.

2 Methods

2.1 Experimental set-up

The mesocosm experiment was carried out in winter (January to ~~–~~March) and fall (October to December) of 2020 at the Sea-ice Environmental Research Facility (SERF; 49.80 °N, 97.14 °W) located on the campus of the University of Manitoba, Winnipeg, Canada, more than 1,800 km south from the Arctic Circle. As the first experimental sea-ice facility in Canada,

85 SERF has been supporting process-oriented~~,~~ mesocosm ~~scale~~ sea ice studies since 2012. It is equipped with an outdoor pool (18.3 m long, 9.1 m wide and 2.6 m deep) exposed to the ambient environment. The pool is filled with artificial seawater (~ 380 m^3) that resembles the salinity and major ionic composition of Arctic seawater. As the air temperature drops well below 0 °C (down to – 30 °C) in winter, the experimental sea ice exhibits similar physical and chemical properties to natural first-year sea ice in the Arctic Ocean (Geilfus et al., 2016; Hare et al., 2013; Xu et al., 2016).

90 For this experiment, ~~The~~the artificial seawater was prepared in November 2019 and formulated by mixing groundwater with concentrated NaCl brine and secondary salts (MgCl$_2$•6H$_2$O, MgSO$_4$•7H$_2$O, CaCl$_2$ and NaBr) to achieve a major-ion composition resembling that of the standard seawater (Millero, 2013) at a salinity of 32.8, including chloride (532.1 mmol kg^{-1}), sulphate (28.4 mmol kg^{-1}), sodium (495.1 mmol kg^{-1}), calcium (10.3 mmol kg^{-1}) and magnesium (33.2 mmol kg^{-1}). To create an amplified signal of bromine activation, excess bromide was added to reach a final concentration of 6.5~~2~~ mmol kg^{-1},

95 which is ~ 8.1~~2~~ times that (0.8~~79~~ mmol kg^{-1}) of a S = 32.8 seawater. Once prepared, the~~The~~ artificial seawater was left to equilibrate with the atmospher~~ice~~ CO$_2$ for more than one month. To prevent it from freezing, seawater was heated from the bottom of the pool and continuously mixed using circulation pumps until the start of the experiment~~s~~. At the end of the equilibration (21 January 2020), the artificial seawater had a pH of 7.8~~75~~, a dissolved inorganic carbon (DIC) concentration of 2500 µmol kg^{-1} and total alkalinity (TA) of 2544 µmol kg^{-1}.

100   In total, four ~~three~~ experiments focusing on different ice or open water stages were carried out. ~~Two of them (~~Experiments #1 and #2~~)~~ followed successive freeze-and-melt cycles of experimental sea ice during ~~the~~ winter (January to March 2020).~~,~~ ~~and the third one (Experiment #3) was carried out in the fall with open water.~~ Experiment #1 started on 21 January when the heater and circulation pumps were turned off. The ice grew naturally until 22 February when the heating on the bottom of the pool was turned on to melt the ice. Open water first appeared on 24 February at which time the circulation pumps ~~was~~were turned on to speed up the melting process. The pool became completely ice free on 2 March. After the heating and circulation pumps were turned off, Experiment #2 started ~~on the same day~~ and continued until 17 March. It followed a natural melting process as the weather warmed up near the end of ~~the e~~Experiment #2. Experiment #3 was carried out in October 2020 for two weeks and the pool remained ice free throughout the duration. Experiment #4 was conducted in December 2020 for one week during the early stage of sea ice formation when the air temperature dropped rapidly.
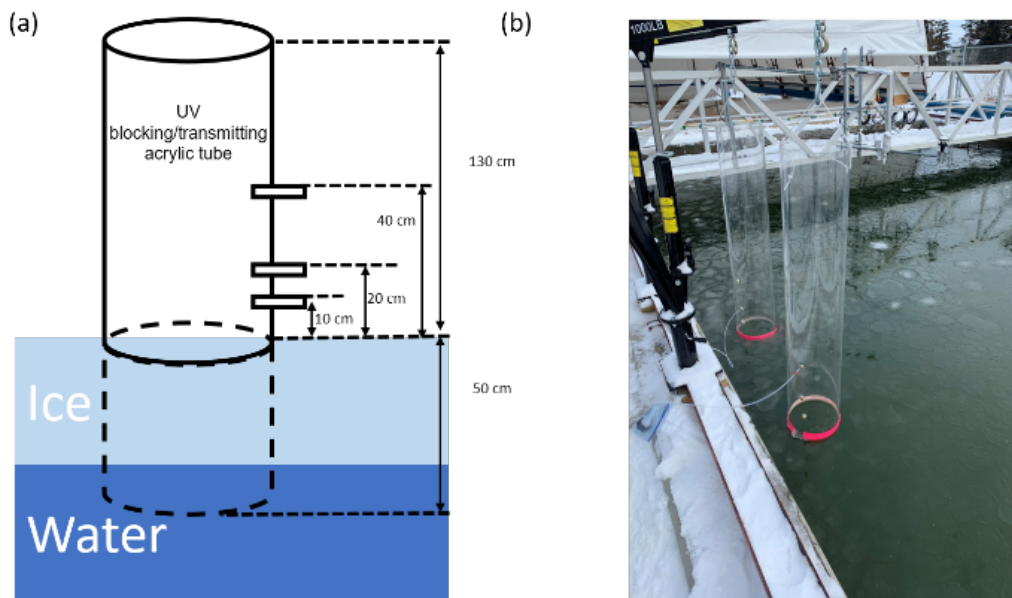
Figure 2. (a) An illustration and (b) a photo showing the experimental set-up at the Sea-ice Environmental Research Facility, Winnipeg, Canada. Two acrylic tubes (one UV-blocking and the other UV-transmitting) were fixed vertically in the sea ice pool, with ozone measurement ports drilled at various heights through the tube wall.

Due to the small surface area of the SERF pool (167 m^2) in an ~~the~~ otherwise urban environment far away from the Arctic, ~~chemical~~ changes induced by chemical reactions in the boundary layer air over the pool can be greatly interfered by the mixing with the ambient air. To limit such air mixing and be able to monitor the change in ~~the~~ ozone concentrations immediately

above the seawater or sea ice surface, two large acrylic tubes (inner diameter: 30 cm, height: 183 cm; Emco Industrial Plastics, Cedar Grove, NJ) were fixed into the seawater before it was frozen, with the bottom 50 cm being submerged in the water. They were placed about 30 cm away from the edge of the pool and were kept vertical by mechanical arms fixed on the edge of the pool (Fig. 2). Both tubes were open to the atmosphere to allow direct air-snow-ice interaction and exchange. One of the tubes wasis made of UV-blocking acrylic material (cut-off wavelength: 370 nm), and the other of UV-transmitting acrylic material (cut-off wavelength: 270 nm) (see Fig. S1 in the Supplementary Information). On each tube, three brass adaptors were drilled through the acrylic wall as sampling ports on the same side located at 10 cm, 20 cm and 40 cm above the water surface, permitting real-time gasozone measurements in the boundary layerin-tube air at different heights (Fig. 2). For the rest of this paper, the "boundary layerin-tube air" is referred to the boundary layer air mass above the sea ice surface constrained inside the acrylic tubes, whereas the air outside of the tubes is considered the "ambient air".

2.2 Ozone and GEM measurements

Real-time ozone concentrations in the boundary layerin-tube air and the ambient air were measured using a Teledyne T400 ozone analyzer which reports averaged ozone concentration forat every minute with a detection limit of 0.4 ppb. The flow rate was 0.8 L min^{-1} through a 4-m heated sample line (inner diameter: 4.8 mm). The ozone analyzer was calibrated at the beginning of the experiment, and frequently checked at a span range of 450 ppb. The relative standard deviation for the span check during the experiments was 2.1 % (n = 11). To allow ozone measurement of the boundary layerin-tube air betweenin different tubes or at different heights above the surface, a two-way switch (Tekran 1100 dual port module) was used to automatically switch between the sampling ports on differentthe two tubes at an interval of 5 minutes. For example, during 12 to 23 February, continuous sampling was conducted at one height on both UV-transmitting and UV-blocking tubes for more than 40 hr before moving to another height for sampling. During data collection at each height, ozone sampling switched between different tubes at an interval of five minutes. Thus, eachthe ozone data reported herein isare averaged over a 5-min integration time (five measurements). The ozone concentrations in the ambient air near the pool were also measured during the experiments.

The quantify and normalize the ozone difference inside the UV-transmitting tube relative to other locations, the ozone loss (%) is reported and calculated by Eq (1):

$$\Delta O_3(\%) = \frac{[O_3]_i - [O_3]_{UVT}}{[O_3]_i} \times 100\% \qquad (1)$$

where $[O_3]_i$ is the ozone concentration in the ambient air or the in-tube air inside the UV-blocking tube, and $[O_3]_{UVT}$ is the ozone concentration in the in-tube air inside the UV-transmitting tube.

During Experiment #4, GEM was also measured in the in-tube air with a 5-min resolution by cold vapour atomic fluorescence spectroscopy (CVAFS) using a Tekran 2537B mercury analyzer; the detection limit was 0.1 ng m^{-3}. The flow rate was 1 L min^{-1} and GEM was monitored using the same sampling system as the ozone measurement. The instrument was

150 routinely calibrated with an internal mercury permeation source and the relative standard deviation was 2.5 % during the experiment (n = 21).

The GEM loss (%) inside the UV-transmitting tube relative to the UV-blocking tube is reported and calculated by Eq (2):

$$\Delta GEM(\%) = \frac{[GEM]_i - [GEM]_{UVT}}{[GEM]_i} \times 100\% \hspace{6cm} (2)$$

where $[GEM]_i$ and $[GEM]_{UVT}$ are the GEM concentrations in the in-tube air inside the UV-blocking tube and inside the UV-
155 transmitting tube, respectively.

2.3 Other measurements

In addition to ozone and GEM, nitrogen oxides (NO, NO_2 and their sum NO_x) concentrations in the ambient air were measured using a Teledyne T200 $NO/NO_2/NO_x$ analyzer near the pool during Experiment #2. The instrument reports data for every minute with a detection limit of 0.4 ppb.

160 Meteorological conditions were measured at a station located at 1.5 m above the ice surface, including air temperature by a Vaisala HMP45C probe, solar irradiance by a CNR4 net radiometer (Kipp & Zonen, spectral range of 0.3–2.8 μm), and wind by an UltraSonic anemometer (WindSonic). In-situ sea ice and seawater temperatures were measured by an automated type-T thermocouple array installed vertically throughout the depth of the pool at a resolution of 2 cm for the top 50 cm.

Seawater, sea ice and snow samples were collected discretely for salinity, major ion composition, pH, DIC and TA
165 analysis. Two ice cores were collected for major ion composition analysis using a Mark II coring system (diameter: 9 cm; KOVACS Enterprise, Roseburg, OR) at the middle and end of Experiment #1 on 10 February and 21 February, respectively. The ice core taken on 21 February was also subsampled for pH analysis. More frequent and separate ice core collection was conducted for DIC and TA measurement. All ice cores were taken from outside of the acrylic tubes within a few meters from where the tubes were located and cut into 3-cm sections immediately after the retrieval. Ice sections were stored in gas-tight
170 plastic bags (Nylon/poly, Cabela's) and vacuum-sealed (Hu et al., 2018), followed by melting at 4 °C in the dark until further analysis. Under-ice water was sampled for major ion composition analysis by submerging 50-mL polypropylene tubes (Falcon) completely underwater from the hole where the ice core was taken, after manually clearing off floating ice. For DIC and TA measurement, the water samples were collected in 100-mL incubation bottles. Multiple snow samples were taken within 48 hr hours after the snow deposition by scooping untouched surface snow on sea ice within the pool area and on the nearby land
175 into 50-mL Falcon tubes. Fresh snow on sea ice was collected within 2 hr after deposition for pH analysis. All snow samples were melted in the dark at 4 °C until further analysis.

Seawater, melted sea ice and snow samples were analyzed for major ion compositions including bromide by ion chromatography (IC) on a DIONEX 5000+ IC system. The recovery and method of detection limit (MDL) were determined from repetitive measurements on a Dionex seven anion standard and a Dionex six cation-II standard, and were 98 % and 1.546
180 μmol kg⁻¹ for bromide, 96 % and 2.01.96 μmol kg⁻¹ for chloride, 99 % and 3.05 μmol kg⁻¹ for sulphate, 97 % and 4.6 μmol

kg^{-1} for nitrite, 95 % and 1.3 µmol kg^{-1} for nitrate, 107 % and 0.2~~0~~ µmol kg^{-1} for sodium, 119 % and 0.8~~79~~ µmol kg^{-1} for magnesium, and 93 % and 1.00~~.95~~ µmol kg^{-1} for calcium. ~~Water aliquots were also collected to measure salinity.~~ Salinity was calculated from conductivity and temperature (Grasshoff et al., 2007), which was measured by a daily-calibrated conductivity cell probe (Orion 013610MD, Thermo Scientific). The pH measurement was carried out on the meltwater of bulk sea ice and snow samples using a daily-calibrated pH glass electrode (Orion 420A, Thermo Scientific).

The analysis of DIC and TA followed the procedure~~process as~~ described in Geilfus et al. (2016). Briefly, ice samples were melted at 4 °C in the dark to minimize the possible dissolution of ikaite crystals. Once sea ice melted, meltwater and seawater were processed similarly by transferring to gas-tight vials (12-mL Exetainers, Labco High Wycombe, UK), preserved with 12 µL ~~solution of~~ saturated HgCl$_2$ solution, and stored at room temperature in the dark until analysis. Total alkalinity was determined by Gran titration (Gran, 1952) on a TIM 840 titration system (Radiometer Analytical, ATS Scientific) (Hu et al., 2018). ~~A 12-mL~~The sample (12 mL) was titrated with a standard 0.05 M HCl solution (Alfa Aesar). Dissolved inorganic carbon was measured on a DIC analyzer (Apollo SciTech) by acidifying a 0.75 mL subsample with 1 mL 10 % H$_3$PO$_4$ (Sigma-Aldrich), followed by quantifying the released CO$_2$ with a CO$_2$ analyzer (LI-COR, LI-7000). Results were then converted from µmol L^{-1} to µmol kg^{-1} based on sample density, which was estimated from salinity and temperature at the time of ~~the~~ analysis. Accuracies of ± 3 and ± 2 µmol kg^{-1} were determined for TA and DIC, respectively, from analysis of certified reference materials (A.G. Dickson, Scripps Institution of Oceanography, USA).

2.4 Statistical analysis

Statistical analysis was carried out using Microsoft Office Excel. One-way ANOVA was used to examine the statistical difference under different occasions and the significant level was set at 0.05 for each test.

3. Results

3.1 Meteorological, sea ice and snow properties

Solar radiation, wind speed and ~~the~~ temperatures of the ambient air, sea ice (when present) and seawater are shown in Figs. 3, 4, and ~~Fig.~~ S2. Throughout Experiments #1 and #2, the presence and vertical extent of sea ice is approximated by the – 2 °C isotherm~~al~~ (Fig. 3c) in the pool.

During Experiment #1 (24 January to 22 February), the ambient air temperature dropped below – 30 °C and the pool surface was completely ice-covered for the entire experiment. The temperature of surface sea ice reached as low as – 16 °C on 19 February. Maximal ice thickness (~ 27 cm) was reached on 21 February near the end of Experiment #1. The daytime that is characterized by a positive downward shortwave radiation was ~ 10 h~~ours~~ (from ~ 8:00 to ~ 18:00; all time local = ~~UTC~~ GMT – 6 hr). During Experiment #2 (3 to 17 March), the ambient air temperature increased gradually from – 20 °C to – 10

210 °C ~~(Fig. 3)~~. The pool surface was only partially ~~sea~~ ice-covered as a result of warming weather that caused interrupted freezing period. The sea ice (when present) thickness was typically less than 10 cm. A longer daytime was observed (~ 11 h~~ours~~), from ~ 7:00 to ~ 18:00. During Experiment #3 (19 to 30 October), no sea ice was observed within the pool. The ambient air temperature ranged from – 8 °C to 4 °C, and the daytime lasted ~ 9.5 h~~ours~~ (from ~ 7:30 to ~ 17:00). During Experiment #4 (9 to 16 December), the pool changed from open water to a complete ice cover and the ice thickness was less than 10 cm. The

215 daytime lasted ~ 7.5 hr (from ~8:30 to ~16:00). The ambient air temperature dropped rapidly from 18 °C on 9 December to below – 10 °C on 14 December.

During Experiments #1 and #2, flurries of snow occurred episodically with less than 1 cm of snow accumulation within the pool area, except on 15 February when up to 5 cm of snow was accumulated on the ice cover outside of acrylic tubes during a snowfall event. The deposited snow went through diel cycle of melting and re-freezing to eventually form a crust

220 layer on the sea ice surface or was blown away from the SERF pool by wind turbulence within 24 h~~ours~~ after deposition. Yet, the accumulated snow layer (< 2 cm) inside the tubes remained visible for several days on the ice surface and inner tube walls as it was sheltered from the ambient wind. During Experiment #4, up to 4 cm of natural snow accumulation inside the tubes were observed above sea ice after snow flurries occurred on the night of 13 December.

3.2 Ozone in the in-tube ~~boundary layer~~ air and ambient air

225 Ozone concentrations in the ambient air and in the ~~boundary layer~~in-tube air inside UV-transmitting and UV-blocking tubes (at 10 cm above the ice surface) are shown in Fig. 3. Large temporal variations in ozone concentrations were found in both the ~~boundary layer~~ in-tube air inside the UV-transmitting tube and ambient air, ranging from 0 to 50 ppb, yet they showed similar temporal patterns. During the overlapped data collection period (17 to 20 February and 3 to 17 March), ozone in the ambient air (32.9 ± 8.5 ppb; mean ± standard deviation) was slightly but significantly higher than that in the ~~boundary layer~~in-

230 tube air measured at 10 cm above the ice surface inside the UV-transmitting tube (30.8 ± 8.2 ppb) ($p < 0.05$~~= 0.00~~). The averaged ozone difference between the UV-transmitting tube and ambient air was 2.3 ± 1.9 ppb for the entire experiment when measurements were done.

Comparisons of ozone concentrations in the in-tube ~~boundary layer~~ air between~~inside~~ UV-transmitting and UV-blocking tubes are shown in Fig. 5~~4~~. Ozone was measured at different heights (10, 20, 40 cm) above the sea ice surface during

235 Experiment #1, whereas during Experiment #3 all ~~the~~ measurements were done at 10 cm above the water surface. The ~~boundary layer~~ozone concentrations in the in-tube air between the two tubes were not significantly different when measured at 40 cm ($p > 0.05$~~= 0.33~~) and 20 cm ($p > 0.05$~~= 0.83~~) above the sea ice surface during Experiment #1 (Fig. 5~~4~~a, b), or at 10 cm above the water surface during Experiment #3 ($p $~~= 0.11~~$> 0.05$) (Fig. 5~~4~~c). The only exception is the measurement conducted closest to the sea ice surface (10 cm) during the ice-covered period in Experiment #1, when the ozone concentration in the UV-

240 transmitting tube was ~~consistently and considerably~~significantly lower than that in the UV-blocking tube (p ~~= 0.00~~< 0.05) (Fig. 5̶4c). The averaged ozone difference between two acrylic tubes at 10 cm above the sea ice surface was 4.6 ± 2.3 ppb.
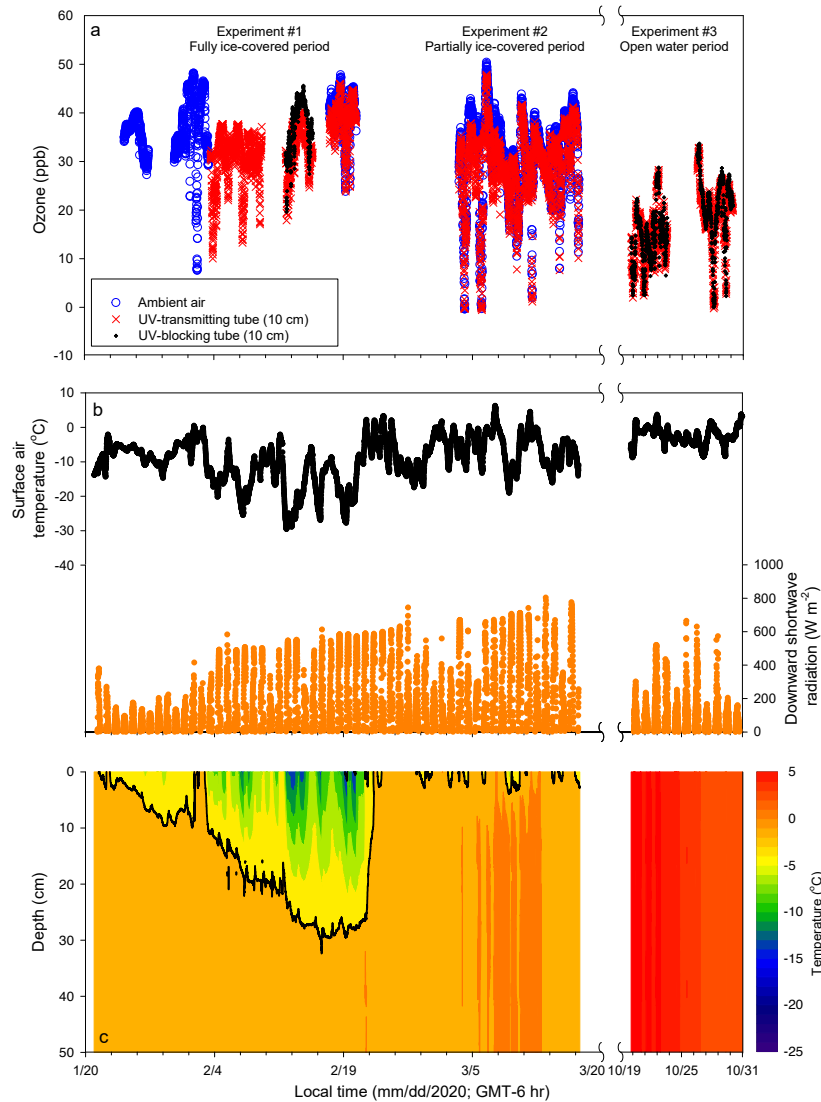
Figure 3. Temporal changes of (a) ozone in the ambient air, and the in-tube air inside the UV-transmitting and UV-blocking tubes (10 cm above the ice or water surface); (b) surface air temperature, solar radiation (1.5 m above the ice or water surface), and (c) ice and water temperatures in the top 50 cm of the pool during Experiments #1, 2 and 3.
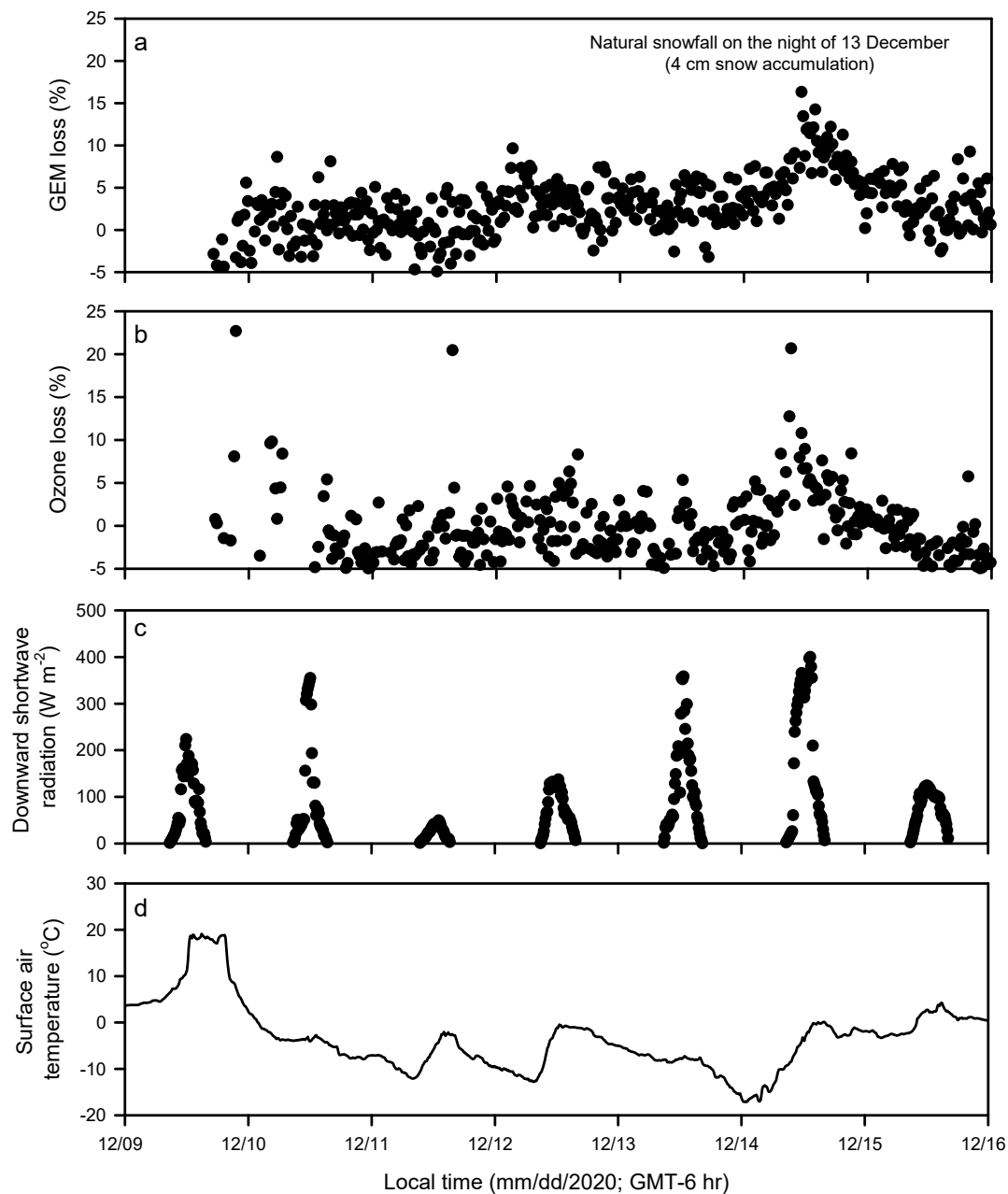
Figure 4. Temporal changes of (a) gaseous elemental mercury (GEM) loss and (b) ozone loss (measured as the difference between the UV-transmitting and UV-blocking tubes), (c) downward shortwave radiation, and (d) surface air temperature during Experiment #4.
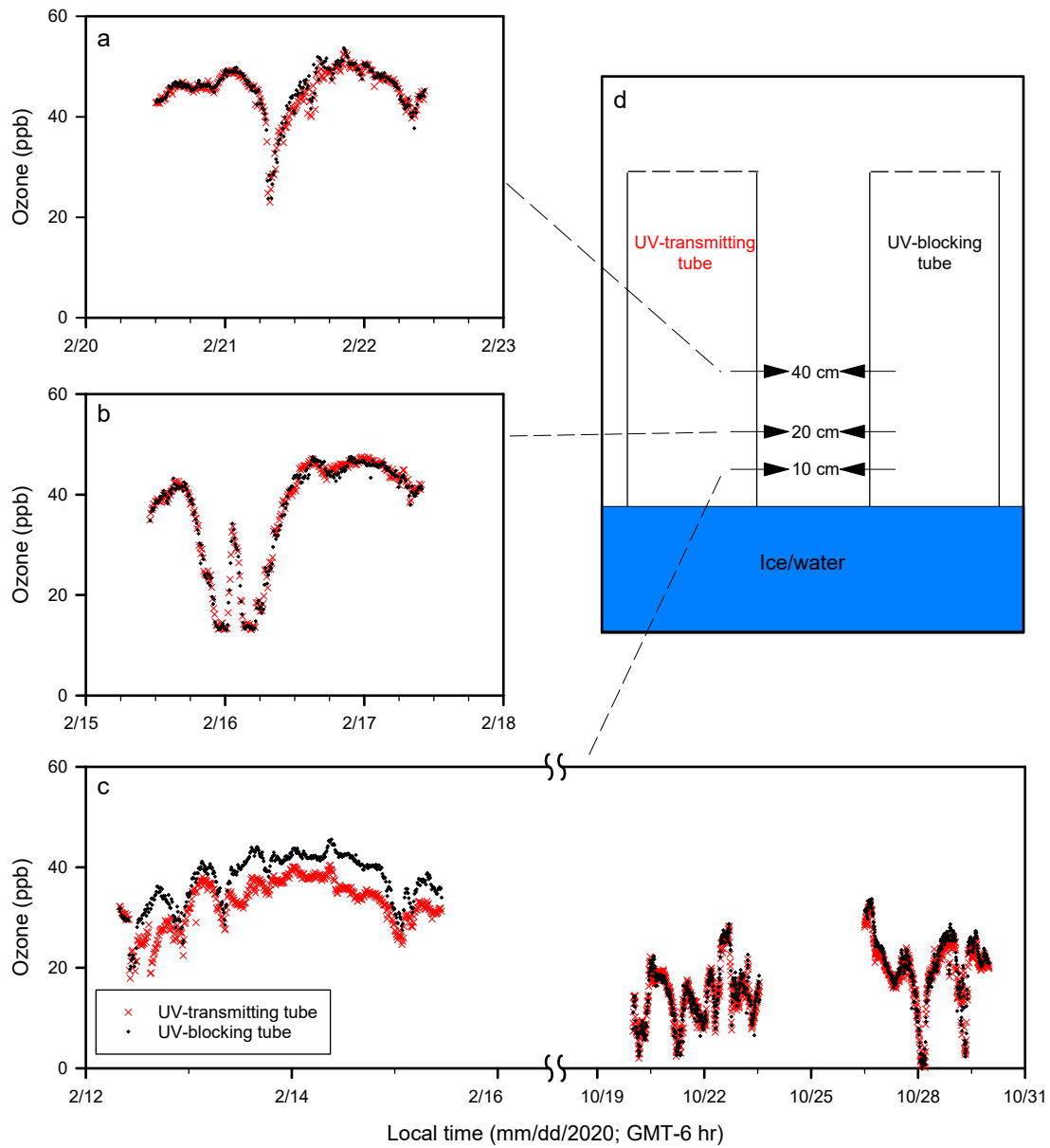
Figure 45. Ozone concentrations in the ~~boundary layer~~in-tube air inside the UV-transmitting and UV-blocking tubes ~~as~~ measured at (a) 40 cm, (b) 20 cm, and (c) 10 cm above the ice (or water) surface. The measurement schemes are illustrated in (d).

3.3 Simultaneous depletion of GEM and ozone in the in-tube air

Both ozone and GEM were measured during Experiment #4 (December 2020). The depletions of GEM (Fig. 4a) and ozone (Fig. 4b) occurred in the same pattern and at the same time. In addition, a larger extent of depletion of both GEM and ozone was observed on December 14 following the accumulation of a thin snow layer (~ 4 cm) above sea ice inside both acrylic tubes the night before.

3.42 Chemical composition of sea ice and snow

The mesocosm experiment was conducted using bromide-enriched artificial seawater. As expected, considerable amounts of ~~major ions~~ salts from seawater are retained in sea ice (Table 1). Ion ~~Major ion~~ concentrations are very low in snow collected from nearby land surfaces, whereas considerably (~ 100 times) higher concentrations are found for the thin layer of snow above sea ice, which is consistent with the brine-wetting process in snow overlying sea ice (Barber and Nghiem, 1999). The exceptions are nitrite and nitrate. Both ions are found to be below the detection limit for almost all the samples except the snow collected from nearby land surfaces. The measured concentrations of bromide and chloride in saline snow and surface sea ice samples were much higher than the values previously reported for Arctic snow samples over first-year and multi-year sea ice (Krnavek et al., 2012; Peterson et al., 2019). This large difference can be explained by a dominant contribution from sea ice brine in our mesocosm experiment, and a more prevalent atmospheric source of halides in natural Arctic snowpack (Peterson et al., 2019). Bromide ~~is of particular interest, which~~ was found to be preferentially enriched in sea ice and in the overlying snow, as demonstrated by elevated $Br^-/$ ~~Na^+~~ Cl^- mol~~e~~ar ratio (0.02~~0 and 0.017, respectively~~) when compared with that in the underlying seawater (0.01~~3~~). Similar preferential enrichment was not observed for other major ions.
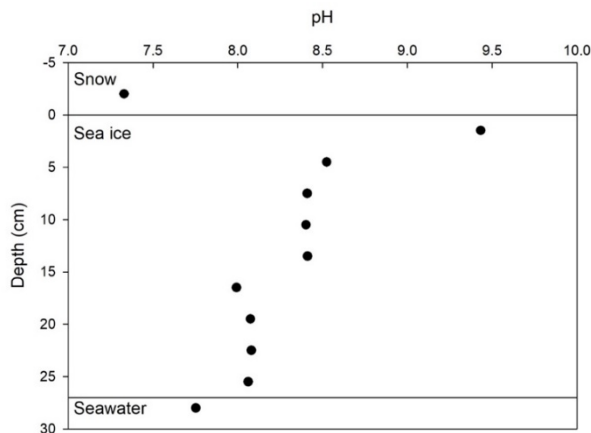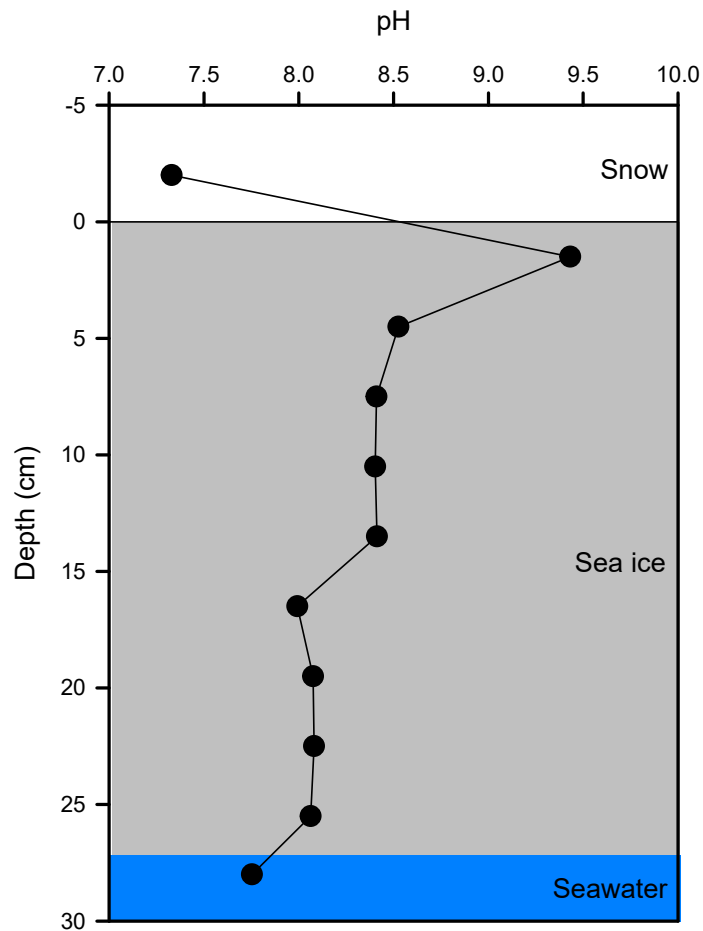
Figure 65. Vertical profile of pH across the snow-sea ice-seawater interface, as measured on the ice core taken on 21 February 2020.

The vertical profile of pH across the snow-sea ice-seawater interface was measured on the ice core taken on 21 February (Fig. 65). The pH of the bulk sea ice meltwater changed from 8.106 at the bottom, to 8.07.99 in the mid-section, and as high as 9.43 near the surface. Estimate based on the measurements of salinity, temperature, DIC and TA (Table 2) suggests that the thin ice and the surface layer of the growing ice consistently had a pH > 8.5 during Experiment #1. Both the high pH values nearat the surface and the C-shaped vertical distribution pattern are in good agreement with those reported in a previous mesocosm study at SERF (Hare et al., 2013). The snow overlying sea ice had a pH of 7.2. It is not as acidic as expected from

that of fresh snow (6.7~~4~~) due to the influence of sea ice brine, but still more than ~~1-2~~ one to two orders of magnitude more acidic than the surface sea ice.

Table 1. Ion ~~Major-ion~~ composition of snow, surface ice and surface seawater during Experiment #1. DL: Detection limit

	Concentration (mmol kg^{-1})								Molar ratio					
	Cl^-	Br^-	SO_4^{2-}	NO_2^-	NO_3^-	Na^+	Mg^{2+}	Ca^{2+}	Br^-/Cl^-	Cl^-/Na^+	Br^-/Na^+	SO_4^{2-}/Na^+	Mg^{2+}/Na^+	Ca^{2+}/Na^+
Snow over land (n=8)	1.5 ± 0.8	0.002 ± 0.001	0.01 ± 0.00	< MDL	0.019 ± 0.005	0.4 ± 0.2	0.02 ± 0.02	0.06 ± 0.02	0.001 ± 0.000	4.8 ± 2.6	0.004 ± 0.001	0.04 ± 0.00	0.06 ± 0.03	0.3 ± 0.1
Snow over sea ice (n=11)	290.4 ± 104.5	4.3 ± 2.1	16.5 ± 5.6	< MDL	< MDL	260.8 ± 95.7	19.8 ± 9.8	5.8 ± 2.2	0.02 ± 0.01	1.1 ± 0.0	0.02 ± 0.01	0.07 ± 0.02	0.07 ± 0.03	0.02 ± 0.00
Sea ice (top 3 cm) (n=4)	269.0 ± 23.0	4.9 ± 1.7	17.9 ± 0.8	< MDL	< MDL	251.2 ± 20.2	18.1 ± 3.0	5.0 ± 0.6	0.02 ± 0.01	1.1 ± 0.0	0.02 ± 0.01	0.07 ± 0.00	0.07 ± 0.01	0.02 ± 0.00
Surface seawater (n=3)	532.1 ± 7.7	6.5 ± 1.1	28.4 ± 1.1	< MDL	< MDL	495.1 ± 1.9	33.2 ± 16.6	10.3 ± 0.2	0.01 ± 0.00	1.1 ± 0.0	0.01 ± 0.00	0.06 ± 0.00	0.07 ± 0.03	0.02 ± 0.00

290

Table 2. Dissolved inorganic carbon (DIC) and total alkalinity (TA) of the seawater and sea ice during Experiment #1

Date	Depth (cm)	Salinity	TA (μmol kg^{-1})	DIC (μmol kg^{-1})
Seawater:				
21 January		32.8	2544	2500
Sea ice:				
22 January	bulk	15.6	1256	1267
24 January	bulk	13.4	1053	877
27 January	bulk	12.3	994	438
30 January	0–4	5.6	484	824
5 February	0–5	7.3	609	518
7 February	0–5	8.0	692	623
10 February	0–5	7.4	670	532
14 February	0–5	9.2	759	604
20 February	0–5	6.3	519	491
24 February	0–5	10.3	844	790

4. Discussion

4.1 Cryo-photochemically driven ozone loss in the in-tube ~~boundary layer~~ air

The temporal variations of ozone concentrations in the ambient air at SERF (Figs. 3a and 7~~6~~a) agree well with those
reported for Canadian cities (Angle and Sandhu, 1989; Raddatz and Cummine, 2001). On a diurnal basis (Fig. 7~~6~~a), the ambient
ozone concentration~~s~~ increase~~s~~ gradually after sunrise (~ 7:30), and peak~~ed~~ around 15:00 to ~~–~~17:00, corresponding to the
production of ozone during photochemical oxidation of hydrocarbons from automobile exhaust, which is also supported by
the variation in downward shortwave radiation (Fig. 7~~6~~c). After sunset, the ambient ozone concentrations increase slightly due
to the inflow of ozone from surrounding rural areas as a result of nocturnal urban heat island effect (Raddatz and Cummine,
2001). In addition, the presence of NO_x would also affect ambient ozone dynamics (Fig. S3) as occasional ozone troughs (near
0 ppb) in the ambient air were observed with NO peaks (Fig. S3a). Similar diurnal patterns of the ozone concentrations are
evident in the ambient air and the ~~boundary layer~~in-tube air inside the UV-transmitting tube even at 10 cm above the sea ice
surface (Fig. 3a and Fig. 7~~6~~a), suggesting that the ozone concentration in the in-tube air is largely controlled by the urban
signal (i.e., the ambient air). However, ozone concentrations in the ambient air are considerably~~consistently~~ higher than that
inside the UV-transmitting tube during sun-lit, daytime (Fig. 7~~6~~a). This could be indicative of limited mixing of the ambient
air inside the tube due to the wall effect, influence on ozone dynamics from NO_x chemistry, and/or loss of ozone inside the
tube due to the presence of the experimental sea ice.

To address which of these processes is primarily responsible for the observed ozone difference, we ~~further~~ investigate the
influence of NO_x chemistry and compare the ozone concentrations measured inside the UV-blocking and UV-transmitting
tubes. The temporal pattern of the ozone difference between the in-tube air inside the UV-transmitting tube and the ambient
air (Fig. S3c) shows the influence of NO_x on the ozone loss (ΔO_3) within the in-tube air is limited. For example, from 11 to 14
March, NO peaks (20 ppb) were observed on 11 March and 14 March, whereas NO stayed at relative low levels (< 3 ppb)
during 12 to 13 March. Yet, during the same time, ΔO_3 within the in-tube air reoccurred daily in a diurnal pattern and reached
a similar extent regardless of NO concentrations. In addition, the in-situ NO_x production via snowpack photochemistry of
nitrate and nitrite is considered negligible due to the low amount of both ions (below the detection limit) found in surface sea
ice and saline snow samples. Thus, NO_x produced either from automobile exhaust or snowpack photochemistry had negligible
influence on ΔO_3 within the in-tube air.

The potential ozone difference caused by the presence of experimental sea ice is further examined by the comparison of
ozone concentrations between UV-blocking and UV-transmitting tubes. ~~Although T~~the overall temporal patterns between the
two tubes we~~a~~re similar during Experiment #1 (Fig. 5~~4~~). Generally~~,~~. the ozone concentration~~s~~ in the in-tube ~~boundary layer~~
air immediately (10 cm) above the sea ice in~~side~~ the UV-transmitting tube were~~are consistently and~~ considerably lower than
those in the UV-blocking tube (Fig. 5~~4~~c). The associated ozone loss (ΔO_3) showe~~ds~~ a clear diurnal pattern with the largest

difference (> 25%) appearing in the early afternoon (12:00 to ~15:00) that correspondeds to the peak time of the downward shortwave radiation (Fig. 87). Since the major difference between the two tubes is their UV-transmitting ability in the range of 270 to 370 nm (Fig. S1) and both tubes were open to the same ambient air mass, the considerable mid-day ozone loss inside the UV-transmitting tube can only be attributed to photochemical processes that are prohibited inside the UV-blocking tube.

The observation that no such ozone loss occurred in the boundary layerin-tube air when measured farther away (20 cm and 40 cm) from the sea ice surface (Fig. 54a, b) suggests that the ozone loss is triggered by cryo-photochemical processes that involve the sea ice environment. At 20 cm or 40 cm above the sea ice surface, the ozone difference between the two tubes becomes indiscernible due to either the faster mixing of the ozone-rich ambient air or the lack of ozone-depleting processes away from the sea ice surface. The importance of cryo-photochemical processes in the ozone loss is further supported by Experiment #3 when the measurement was conducted in the absence of sea ice, ands no ozone loss was observed even immediately (10 cm) above the water surface (Fig. 56c and Fig. 8c).

Since the UV-transmitting tube only has a UV transmittance of ~ 60% (Fig. S1), even higher magnitude of the ozone loss is expected to occur outside of the acrylic tubes over the entire SERF sea ice surface. However, the rapid mixing of the boundary layer air and the ambient air would readily bury the ozone-depleting signal under the much larger background of ambient urban air, making it difficult to directly observe such cryo-photochemical ozone loss. The use of the acrylic tubes is thus critical for the observation, as they limited the air mixing and permitted gas sampling from the boundary layerin-tube air mass that was directly affected by the sea ice surface. Moreover, comparing ozone concentrations between tubes cancels out the variations that exist in the ambient air since both tubes were open to the same air mass and the ozone dynamics in the ambient air should be equally applied to both tubes.

It should also be noted that the relationship between the intensity of downward shortwave radiation and the extent of the cryo-photochemical ozone loss is yet to be validated (Fig. 4 and Fig. S4). The lack of correlation may be explained by the fact that the downward shortwave radiation reported in this study covers wavelength from 300 nm to 2800 nm, whereas UV radiation (< 400 nm) has been generally considered the most effective range causing photochemical ozone loss. Other factors, such as the presence of various condensed phase, the availability of Br^- substrates and air temperatures would also affect the extent of the cryo-photochemical ozone loss.

4.2 Mesocosm reproduction of Arcticpolar springtime photochemical phenomena

Although no direct measurements were made in this study on gas-phase bromine species in the air above sea ice or snow, we believe the simultaneous cryo-photochemical ozone and GEM loss observed over the SERF pool (Fig. 4) are is caused by the same mechanism involving bromine activation that is responsible for the Arctic springtime ODEs and MDEs. The other known tropospheric ozone depletion mechanisms include direct photolysis (Schmidt et al., 2016; Wu et al., 2007), NO_x

chemistry (Nakayama et al., 2015) and ozone deposition on the tube walls, which are negligible at the study site as demonstrated by a lack of ozone loss during the early fall (see Fig. 8̶7c).
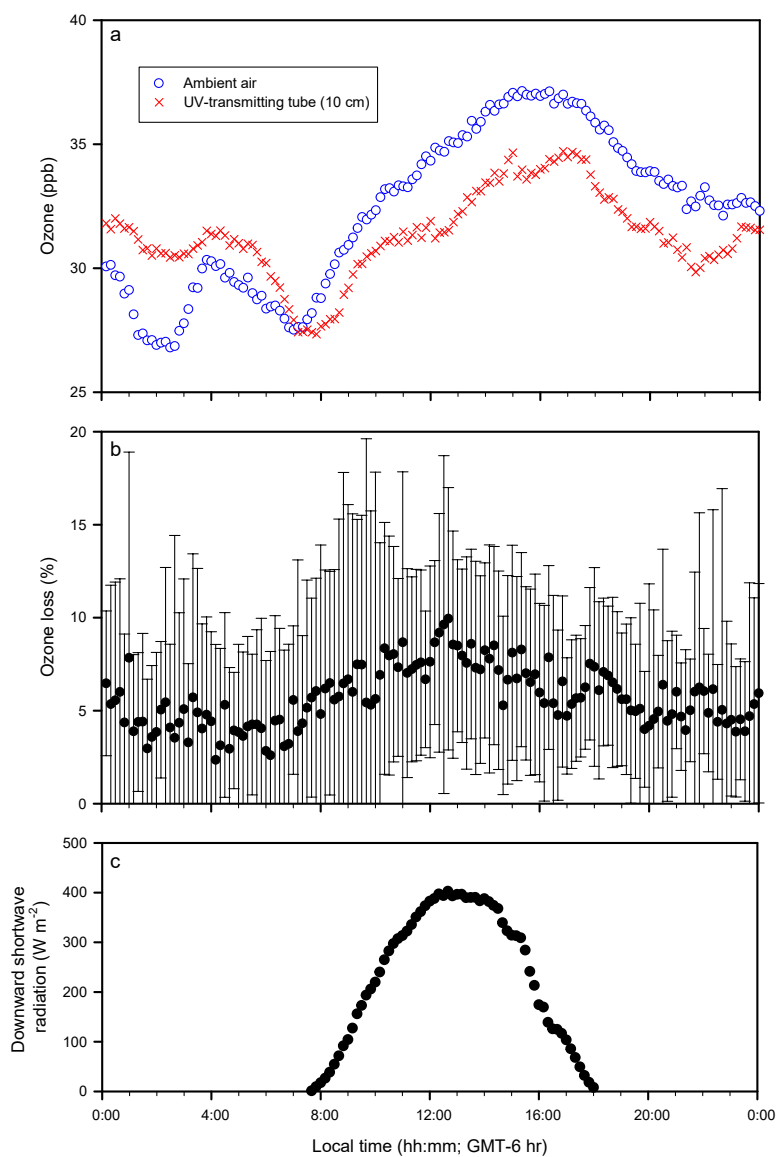
355

Figure 7̶6. Diurnal patterns (averaged over 24 January to 17 March whenever the measurement was available) of (a) ozone concentrations in the ambient air and ~~boundary layer~~the in-tube air inside the UV-transmitting tube (10 cm above the sea ice), (b) ozone loss (%) (measured as the ozone ~~concentration~~ difference between the ambient air and ~~boundary layer~~the in-tube air inside the UV-transmitting tube), and (c) downward shortwave radiation.
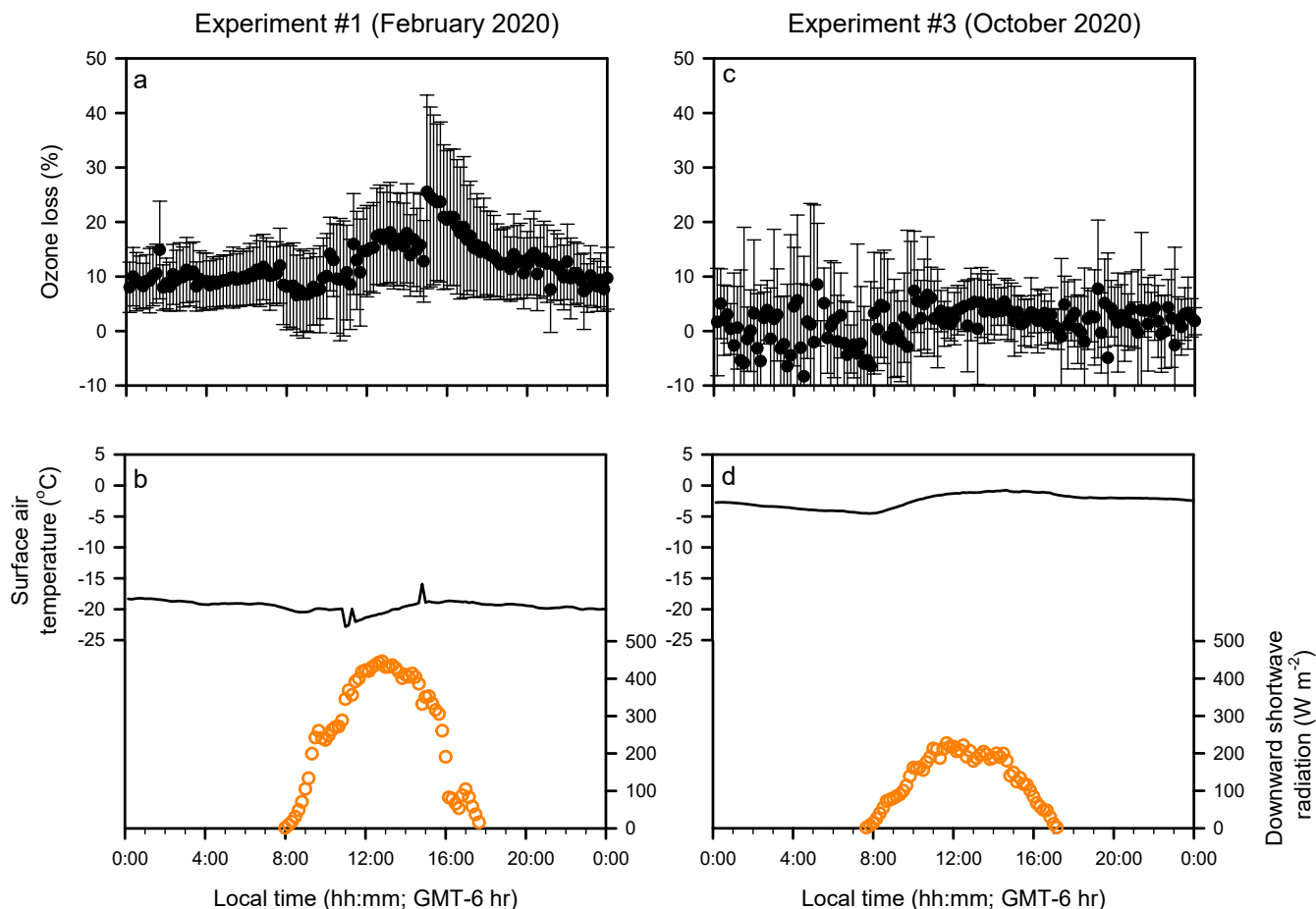
Figure 87. Diurnal patterns of (a, c) ozone loss (%) (measured as the ozone concentration difference in the boundary layerin-tube air between the UV-transmitting and UV-blocking tubes at 10 cm above the sea ice or water surface), and (b, d) meteorological conditions during the ice-covered (a, b) and open water (b, d) experiments.

As shown in Fig. 1, Br radicals-induced cryo-photochemical ozone and GEM loss involves multi-phase reactions on the surface of a condensed phase under acidic conditions (Abbatt et al., 2012; Pratt et al., 2013; Simpson et al., 2007). The condensed phase can be either the bare sea ice or the thin layer of snow accumulated on the sea ice surface at the second half of Experiment #1 and during Experiment #4. The measured Br⁻/Cl⁻ ratios in saline snow and in surface sea ice samples (0.02) are found to be in favour of active cycling of bromine species. Pratt et al. (2013) suggested an optimal Br⁻/Cl⁻ mole ratio

threshold for Br$_2$ production of 0.005, which is below our observed ratios for the potential condensed phase reactors. However, the highly alkaline nature of the sea ice surface (Fig. 65; see also Hare et al., 2013) suggests it is not the most efficient surface where brominebromide activation takes place. Instead, the overlying snow is more likely acting as a more favourablethe

375   condensed phase for the reactions to take place. The importance of the snow layer was further demonstrated during Experiment #4 when stronger ODEs and MDEs were observed shortly after the accumulation of the snow layer on sea ice. The snow layer overlying sea ice, as it is more acidic (Fig. 65) yet enriched in bromide (Table 1) due to the upward migration of sea ice brine. As shown in Table 1, the bromide added in the artificial seawater eventually contributed to enriched bromide concentrations found in sea ice surface and the overlying snow layerpack, providing abundant substrates for bromine activation. Furthermore,

380   the occurrence of BEEs is indicated by the observation of concurrent ODEs and MDEs (Fig. 4a, b) in the mesocosm.

5. Conclusion

In this paper, we show that the Arctic springtime ODEs and MDEs can be reproduced in a mesocosm-scale experiment in an outdoor, mesocosm sea ice facility located in an urban area far away from the Arctic. By constraining the boundary layer air mass within a UV-transmittingacrylic tubes, cryo-photochemical ozone and GEM loss above experimental sea ice areis

385   observed with a diurnal pattern that is characteristic of BEE-induced ODEsphotochemical phenomena. Meanwhile, simultaneous occurrences of both ODEs and MDEs are observed in the in-tube air near the sea ice and snow surface. The comparison between the UV-blocking and UV-transmitting acrylic tubes further emphasizes the role of UV radiation (270 to 370 nm) in causing these photochemical phenomena such ozone destruction.

Several improvements can be made for future studies. Even though organic matter and biota were not intentionally

390   introduced into the mesocosm, some of them could have made into the system; to which extent they could have influenced the cryo-photochemical processes (e.g., via the production of bromocarbons) warrants further exploration. Another aspect is related to ice-nucleating particles which are likely to affect the roughness of the sea ice surface and assist in frost formation on the tube walls during mornings, which could potentially act as a temporary condensed phase for bromine activation just after sunrise. Time-series measurements of pH at the air-ice/snow interface could also be explored to probe the availability of

395   protons and the efficiency of HOBr dissociation on the surface of sea ice or snow layer.

The success in reproducing BEE-induced ODEs at the mesocosm scalephotochemical phenomena in a mesocosm experiment provides a new approach that can supplement, bridge and integrate the laboratory and field-scale studies to advance our understanding of the cryo-photochemical processes and meteorological conditions processesleading to BEEs, ODEs, and MDEs in the Arctic. In addition to much simpler logistical preparations, major advantages of the mesocosm-scale approach

400   are the ability to control and modify the nature and dynamics of various condensed phases (e.g., sea ice, frost flowers, open leads, overlying snow and blowing snow under various growth and melting conditions), the ability to dope or alter chemical

composition of seawater and condensed phases (e.g., addition of bromide and mercury stable isotopes, acidity), the ability to control the light environment, and the accessibility to various monitoring and analytical capacities (e.g., those for bromocarbons, ice-nucleating particles) that are difficult to access in the remote Arctic. The results will not only help fill up critical knowledge gaps related to BEEs, ODEs and MDEs, but also aid the development and parameterization of mechanistic models to allow better projection of their sensitivities to climate change in the Arctic, and better understanding of implications for biogeochemical cycles across the ocean-sea ice-atmosphere interfaces.

Data availability

The datasets generated in this study are available on request from the corresponding author.

Author contribution

ZG and FW designed the experiments and led the data interpretation. ZG and NXG carried out the experiments. ASL assisted in data interpretation. ZG and FW prepared the manuscript with contributions from all co-authors.

Competing interests

The authors declare that they have no conflict of interest.

Acknowledgements

This work was funded by the Natural Science and Engineering Council of Canada (NSERC), the Canada Research Chairs program, the Canada Excellence Research Chairs (CERC) program, and the University of Manitoba Graduate Fellowship. We thank D. Armstrong for assistance in thee major ion chromatography analysis, and D. Binne for assistance in the experimentation at the Sea-ice Environmental Research Facility (SERF). We thank two anonymous referees and Editor J. Kuttippurath for their constructive comments during the peer-review process.

References

Abbatt, J., Oldridge, N., Symington, A., Chukalovskiy, V., McWhinney, R. D., Sjostedt, S. and Cox, R. A.: Release of gas-phase halogens by photolytic generation of OH in frozen halide-nitrate solutions: An active halogen formation mechanism? J. Phys. Chem. A, 114, 6527–6533, https://doi.org/10.1021/jp102072t, 2010.

425 Abbatt, J. P. D., Thomas, J. L., Abrahamsson, K., Boxe, C., Granfors, A., Jones, A. E., King, M. D., Saiz-Lopez, A., Shepson, P. B., Sodeau, J., Toohey, D. W., Toubin, C., von Glasow, R., Wren, S. N. and Yang, X.: Halogen activation via interactions with environmental ice and snow in the polar lower troposphere and other regions, Atmos. Chem. Phys., 12, 6237–6271, https://doi.org/10.5194/acp-12-6237-2012, 2012.

Angle, R. P. and Sandhu, H. S.: Urban and rural ozone concentrations in Alberta, Canada, Atmos. Environ., 23, 215–221,
430 https://doi.org/10.1016/0004-6981(89)90113-3, 1989.

Barber, D. G. and Nghiem, S. V.: The role of snow on the thermal dependence of microwave backscatter over sea ice, J. Geophys. Res. Ocean., 104, 25789–25803, https://doi.org/10.1029/1999jc900181, 1999.

Barrie, L. and Platt, U.: Arctic tropospheric chemistry: An overview, Tellus , Ser. B Chem. Phys. Meteorol., 49, 450–454, https://doi.org/10.3402/tellusb.v49i5.15984, 1997.

435 Barrie, L. A., Bottenheim, J. W., Schnell, R. C., Crutzen, P. J. and Rasmussen, R. A.: Ozone destruction and photochemical reactions at polar sunrise in the lower Arctic atmosphere, Nature, 334, 138–141, https://doi.org/10.1038/334138a0, 1988.

Bognar, K., Zhao, X., Strong, K., Chang, R. Y. W., Frieß, U., Hayes, P. L., McClure-Begley, A., Morris, S., Tremblay, S. and Vicente-Luis, A.: Measurements of tropospheric bromine monoxide over four halogen activation seasons in the Canadian High Arctic, J. Geophys. Res. Atmos., 125, 1–23, https://doi.org/10.1029/2020JD033015, 2020.

440 Bottenheim, J. W., Gallant, A. G. and Brice, K. A.: Measurements of NO_Y species and O_3 at 82° N latitude, Geophys. Res. Lett., 13, 113–116, https://doi.org/10.1029/GL013i002p00113, 1986.

Burd, J. A., Peterson, P. K., Nghiem, S. V., Perovich, D. K. and Simpson, W. R.: Snowmelt onset hinders bromine monoxide heterogeneous recycling in the Arctic, J. Geophys. Res. Atmos, 122, https://doi.org/10.1002/2017JD026906, 2017.

Geilfus, N. X., Galley, R. J., Else, B. G. T., Campbell, K., Papakyriakou, T., Crabeck, O., Lemes, M., Delille, B. and Rysgaard,
445 S.: Estimates of ikaite export from sea ice to the underlying seawater in a sea ice-seawater mesocosm, Cryosphere, 10, 2173–2189, https://doi.org/10.5194/tc-10-2173-2016, 2016.

Gran, G.: Determination of the equivalence point in potentiometric titrations. Part II, Analyst, 77, 661–670, https://doi.org/10.1039/AN9527700661, 1952.

Grasshoff, K., Kremling, K. and Ehrhardt, M.: Methods of Seawater Analysis, Third Edition, Wiley-VCH, Weinheim, 2007.

450 Halfacre, J. W., Shepson, P. B. and Pratt, K. A.: PH-dependent production of molecular chlorine, bromine, and iodine from frozen saline surfaces, Atmos. Chem. Phys., 19, https://doi.org/10.5194/acp-19-4917-2019, 2019.

Hare, A. A., Wang, F., Barber, D., Geilfus, N. X., Galley, R. J. and Rysgaard, S.: pH evolution in sea ice grown at an outdoor experimental facility, Mar. Chem., 154, 46–54, https://doi.org/10.1016/j.marchem.2013.04.007, 2013.

Hu, Y. Bin, Wang, F., Boone, W., Barber, D. and Rysgaard, S.: Assessment and improvement of the sea ice processing for
455 dissolved inorganic carbon analysis, Limnol. Oceanogr. Methods, 16, 83–91, https://doi.org/10.1002/lom3.10229, 2018.

Huff, A. K. and Abbatt, J. P. D.: Kinetics and product yields in the heterogeneous reactions of HOBr with ice surfaces containing NaBr and NaCl, J. Phys. Chem. A, 106, 5279–5287, https://doi.org/10.1021/jp014296m, 2002.

Khiri, D., Louis, F., Černušák, I. and Dibble, T. S.: BrHgO• + CO: Analogue of OH + CO and reduction path for Hg(II) in the atmosphere, ACS Earth Space Chem., 4, https://doi.org/10.1021/acsearthspacechem.0c00171, 2020.

460 Krnavek, L., Simpson, W. R., Carlson, D., Domine, F., Douglas, T. A. and Sturm, M.: The chemical composition of surface snow in the Arctic: Examining marine, terrestrial, and atmospheric influences, Atmos. Environ., 50, 349–359, https://doi.org/10.1016/j.atmosenv.2011.11.033, 2012.

Millero, F. J.: Chemical Oceanography, Fourth Edition, CRC Press, Boca Raton, 2013.

Moore, C. W., Obrist, D., Steffen, A., Staebler, R. M., Douglas, T. A., Richter, A. and Nghiem, S. V.: Convective forcing of 465 mercury and ozone in the Arctic boundary layer induced by leads in sea ice, Nature, 506, 81–84, https://doi.org/10.1038/nature12924, 2014.

Nakayama, M., Zhu, C., Hirokawa, J., Irino, T. and Yoshikawa-Inoue, H.: Ozone depletion in the interstitial air of the seasonal snowpack in northern Japan, Tellus B, 67, https://doi.org/10.3402/tellusb.v67.24934, 2015.

Oltmans, S. J. and Komhyr, W. D.: Surface ozone distributions and variations from 1973–1984: Measurements at the NOAA 470 geophysical monitoring for climatic change baseline observatories, J. Geophys. Res., 91, 5229, 5229–5236, https://doi.org/10.1029/jd091id04p05229, 1986.

Oltmans, S. J., Schnell, R. C., Sheridan, P. J., Peterson, R. E., Li, S. M., Winchester, J. W., Tans, P. P., Sturges, W. T., Kahl, J. D. and Barrie, L. A.: Seasonal surface ozone and filterable bromine relationship in the high Arctic, Atmos. Environ., 23, 2431–2441, https://doi.org/10.1016/0004-6981(89)90254-0, 1989.

475 Peterson, P. K., Hartwig, M., May, N. W., Schwartz, E., Rigor, I., Ermold, W., Steele, M., Morison, J. H., Nghiem, S. V. and Pratt, K. A.: Snowpack measurements suggest role for multi-year sea ice regions in Arctic atmospheric bromine and chlorine chemistry, Elementa, 7, https://doi.org/10.1525/elementa.352, 2019.

Platt, U. and Hausmann, M.: Spectroscopic measurement of the free radicals NO_3, BrO, IO, and OH in the troposphere, Res. Chem. Intermed., 20, 557–578, https://doi.org/10.1163/156856794X00450, 1994.

480 Pratt, K. A., Custard, K. D., Shepson, P. B., Douglas, T. A., Pöhler, D., General, S., Zielcke, J., Simpson, W. R., Platt, U., Tanner, D. J., Gregory Huey, L., Carlsen, M. and Stirm, B. H.: Photochemical production of molecular bromine in Arctic surface snowpacks, Nat. Geosci., 6, 351–356, https://doi.org/10.1038/ngeo1779, 2013.

Raddatz, R. L. and Cummine, J. D.: Temporal surface ozone patterns in urban Manitoba, Canada, Boundary-Layer Meteorol., 99, 411–428, https://doi.org/10.1023/A:1018983012168, 2001.

485 Saiz-Lopez, A. and von Glasow, G.: Reactive halogen chemistry in the troposphere, Chem. Soc. Rev., 41, 6448–6472, https://doi.org/10.1039/c2cs35208g, 2012.

Schmidt, J. A., Jacob, D. J., Horowitz, H. M., Hu, L., Sherwen, T., Evans, M. J., Liang, Q., Suleiman, R. M., Oram, D. E., Le Breton, M., Percival, C. J., Wang, S., Dix, B. and Volkamer, R.: Modeling the observed tropospheric BrO background: Importance of multiphase chemistry and implications for ozone, OH, and mercury, J. Geophys. Res., 121, 11819–11835, https://doi.org/10.1002/2015JD024229, 2016.

Schroeder, W. H., Anlauf, K. G., Barrie, L. A., Lu, J. Y., Steffen, A., Schneeberger, D. R. and Berg, T.: Arctic springtime depletion of mercury, Nature, 394, 331–332, https://doi.org/10.1038/28530, 1998.

Simpson, W. R., Brown, S. S., Saiz-Lopez, A., Thornton, J. A. and von Glasow, R.: Tropospheric halogen chemistry: sources, cycling, and impacts, Chem. Rev., 115, 4035–4062, https://doi.org/10.1021/cr5006638, 2015.

Simpson, W. R., Carlson, D., Hönninger, G., Douglas, T. A., Sturm, M., Perovich, D. and Platt, U.: First-year sea-ice contact predicts bromine monoxide (BrO) levels at Barrow, Alaska better than potential frost flower contact, Atmos. Chem. Phys., 7, 621–627, https://doi.org/10.5194/acp-7-621-2007, 2007a.

Simpson, W. R., von Glasow, R., Riedel, K., Anderson, P., Ariya, P., Bottenheim, J., Burrows, J., Carpenter, L. J., Frieß, U., Goodsite, M. E., Heard, D., Hutterli, M., Jacobi, H. W., Kaleschke, L., Neff, B., Plane, J., Platt, U., Richter, A., Roscoe, H., Sander, R., Shepson, P., Sodeau, J., Steffen, A., Wagner, T. and Wolff, E.: Halogens and their role in polar boundary-layer ozone depletion, Atmos. Chem. Phys., 7, 4375–4418, https://doi.org/10.5194/acp-7-4375-2007, 2007b.

Sjostedt, S. J. and Abbatt, J. P. D.: Release of gas-phase halogens from sodium halide substrates: Heterogeneous oxidation of frozen solutions and desiccated salts by hydroxyl radicals, Environ. Res. Lett., 3, https://doi.org/10.1088/1748-9326/3/4/045007, 2008.

Steffen, A., Schroeder, W., Macdonald, R., Poissant, L. and Konoplev, A.: Mercury in the Arctic atmosphere: An analysis of eight years of measurements of GEM at Alert (Canada) and a comparison with observations at Amderma (Russia) and Kuujjuarapik (Canada), Sci. Total Environ., 342, 185–198, https://doi.org/10.1016/j.scitotenv.2004.12.048, 2005.

Thomas, J. L., Stutz, J., Lefer, B., Huey, L. G., Toyota, K., Dibb, J. E. and von Glasow, R.: Modeling chemistry in and above snow at Summit, Greenland - Part 1: Model description and results, Atmos. Chem. Phys., 11, 4899–4914, https://doi.org/10.5194/acp-11-4899-2011, 2011.

Wang, F., Pućko, M. and Stern, G.: Transport and transformation of contaminants in sea ice, in Sea Ice: Third Edition, Edited by D.N. Thomas, John Wiley & Sons, pp. 472–491, https://doi.org/10.1002/9781118778371.ch19, 2017.

Wang, S., McNamara, S. M., Moore, C. W., Obrist, D., Steffen, A., Shepson, P. B., Staebler, R. M., Raso, A. R. W. and Pratt, K. A.: Direct detection of atmospheric atomic bromine leading to mercury and ozone depletion, Proc. Natl. Acad. Sci. U. S. A., 116, 14479–14484, https://doi.org/10.1073/pnas.1900613116, 2019.

Wang, S. and Pratt, K. A.: Molecular Halogens Above the Arctic Snowpack: Emissions, Diurnal Variations, and Recycling Mechanisms, J. Geophys. Res. Atmos., 122, https://doi.org/10.1002/2017JD027175, 2017.

Wren, S. N., Donaldson, D. J. and Abbatt, J. P. D.: Photochemical chlorine and bromine activation from artificial saline snow, Atmos. Chem. Phys., 13, 9789–9800, https://doi.org/10.5194/acp-13-9789-2013, 2013.

520   Wu, S., Mickley, L. J., Jacob, D. J., Logan, J. A., Yantosca, R. M. and Rind, D.: Why are there large differences between models in global budgets of tropospheric ozone?, J. Geophys. Res. Atmos., 112, 1–18, https://doi.org/10.1029/2006JD007801, 2007.

Xu, W., Tenuta, M. and Wang, F.: Bromide and chloride distribution across the snow-sea ice-ocean interface: A comparative study between an Arctic coastal marine site and an experimental sea ice mesocosm, J. Geophys. Res. Ocean., 121, 5535–

525   5548, https://doi.org/10.1002/2015JC011409, 2016.

Zhao, X., Strong, K., Adams, C., Schofield, R., Yang, X., Richter, A., Friess, U., Blechschmidt, A. M. and Koo, J. H.: A case study of a transported bromine explosion event in the Canadian high arctic, J. Geophys. Res. Atmos., 121, 457–477, https://doi.org/10.1002/2015JD023711, 2016.